3D Imaging Spectroscopy for Measuring Hyperspectral Patterns on Solid Objects

Min H. Kim[†]

Todd Alan Harvey[♮]

David S. Kittle[§]

Holly Rushmeier[†]   Julie Dorsey[†]

Richard O. Prum[♮*]

David J. Brady[§]

Yale University
Computer Science[†]

Yale Unversity
Ecology & Evolutionary Biology[♮]
Peabody Museum of Natural History[*]

Duke University
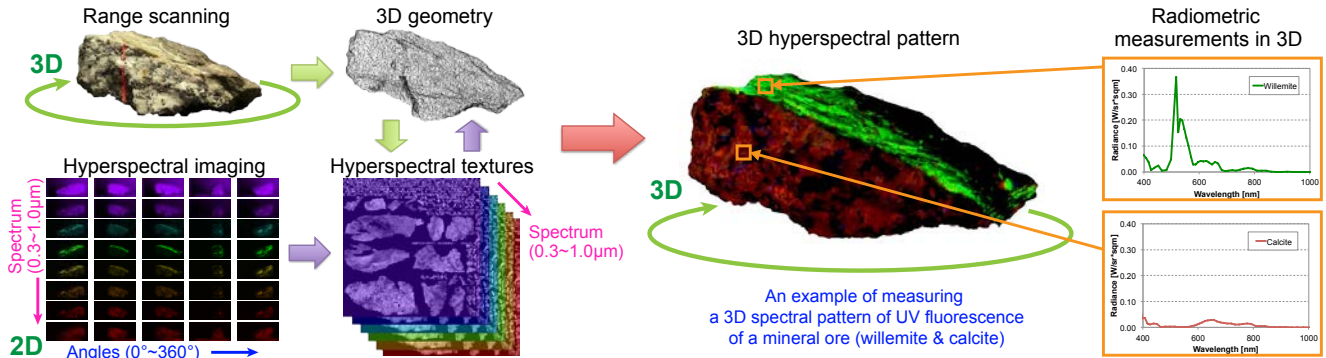Electrical & Computer Engineering[§]

Figure 1: *An overview of our system for measuring a three-dimensional (3D) hyperspectral pattern on a solid object. Our 3D imaging spectroscopy (3DIS) system measures 3D geometry and hyperspectral radiance simultaneously. Piecewise geometries and radiances are reconstructed into a 3D hyperspectral pattern by our reconstruction pipeline. Our system is used to measure physically-meaningful 3D hyperspectral patterns of various wavelengths for scientific research.*

Abstract

Sophisticated methods for true spectral rendering have been developed in computer graphics to produce highly accurate images. In addition to traditional applications in visualizing appearance, such methods have potential applications in many areas of scientific study. In particular, we are motivated by the application of studying avian vision and appearance. An obstacle to using graphics in this application is the lack of reliable input data. We introduce an end-to-end measurement system for capturing spectral data on 3D objects. We present the modification of a recently developed hyperspectral imager to make it suitable for acquiring such data in a wide spectral range at high spectral and spatial resolution. We capture four megapixel images, with data at each pixel from the near-ultraviolet (359 nm) to near-infrared (1,003 nm) at 12 nm spectral resolution. We fully characterize the imaging system, and document its accuracy. This imager is integrated into a 3D scanning system to enable the measurement of the diffuse spectral reflectance and fluorescence of specimens. We demonstrate the use of this measurement system in the study of the interplay between the visual capabilities and appearance of birds. We show further the use of the system in gaining insight into artifacts from geology and cultural heritage.

Links: ◆DL 🗎PDF

1 Introduction

Physically-based full-spectral rendering has long been recognized as an important area in computer graphics and has received considerable attention [Devlin et al. 2002]. Systems have been developed that are capable of producing images of stunning visual quality [Next-Limit-Technologies 2012]. However, there are many additional applications of spectral rendering in scientific study that have yet to be explored. A primary example of such an application is the investigation of the development of animal vision systems and appearance. The obstacle to applying advanced computer graphics methods in this area is the lack of reliable spectral reflectance data for 3D specimens. In this paper we present a complete measurement system for obtaining such spectral data. Specifically motivated by the study of avian vision, we describe the development of a 3D scanning system that incorporates a hyperspectral imager that captures four megapixel images with spectral data at ~12 nm resolution in the range of near-ultra violet (359 nm) to near-infrared (1,003 nm).

Our system employs both dispersion- and bandpass-based imaging to overcome limitations in spectral and spatial resolution in previous hyperspectral imaging systems. The imager is integrated into a 3D scanning pipeline (with a triangulation-based 3D range scanner) to complete the radiometric measurement of the entire surface of a 3D object. In particular, our system focuses on radiometric accuracy in measuring diffuse reflectance and fluorescence of the surfaces of a 3D solid object. As a scientific instrument, our system rivals the accuracy and spectral resolutions of commodity spectrometers. Our system measures radiometric properties in 3D, rather than via 2D flat surfaces, greatly expanding the range of applications that can benefit from hyperspectral measurement.

More faithful representations of surface reflectance are crucial to many applications besides our motivating example of avian vision. In addition to birds, we consider example applications in geology and cultural heritage. In both of these applications accurate spectral signatures are valuable in the analysis and identification of materials.

We make the following contributions:

- integration of 2D imaging spectroscopy and 3D scanning enabling the measurement of physically-meaningful *3D hyperspectral patterns* of arbitrarily-shaped solid objects with high accuracy,

- modification of a previous hyperspectral imager to achieve high spatial and spectral resolution essential for reconstructing 3D hyperspectral patterns,

- characterization of our system to measure physically-meaningful 3D hyperspectral patterns, rivaling the spectral resolution and accuracy of commodity spectrometers, and

- demonstration of the 3DIS instrument for acquiring hyperspectral reflectance and fluorescence for shapes from natural science and cultural heritage.

2 Background and Previous Work

In this section we briefly overview previous work in 3D and spectral measurements.

Shape and Appearance Capture Reconstructing a color 3D model from multiple overlapping geometry scans has been an active area for many years in computer graphics. Bernardini and Rushmeier [2002] summarized the general 3D scanning pipeline that has been employed by many research projects and commercial systems. In general, a 3D scanning system (typically a triangulation system for small objects, or time-of-flight system for building scale structures) is coupled with a color camera system and lights. The camera and lights are either mechanically coupled to the 3D scanner, or the relationship between camera, lights and scanner are determined in a registration post-process. Early systems for capturing object shape and appearance include Farouk et al. [2003] and Lensch et al. [2003]. More recently Holroyd et al. [2010] have presented a sophisticated system for using a digital camera and spatially modulated light source to extract both shape and appearance from the same set of images. Holroyd et al. measure bidirectional RGB reflectance, exploring directional changes. Our system focuses on spectral dimensionality and adapts compressive sensing into a 3D scanning system.

A straightforward approach to 3D scanning with hyperspectral reflectance measurement would simply swap out the standard RGB camera used in current scanning systems and replace them with a hyperspectral device. Such an approach is described in seminal papers, e.g., Brusco et al. [2006] and Mansouri et al. [2007]. Brusco et al. illustrated hyperspectral images registered with 3D captured data to reconstruct a segment of a frescoed wall. The work showed that this approach is useful for monitoring oxidation and aging for the purpose of architectural conservation. However, the imaging system was limited in spatial resolution and spectral range and hampered by lengthy capture time. In addition, the calibration accuracy of the structural light source and coaxial camera in a modern system such as Holroyd et al. relies on the spatial resolution of the camera, which is low in hyperspectral cameras. For sensing UV fluorescence in 3D, high frequency structured light cannot be accurately reflected because of subsurface scattering inside the excited substrate.

The key missing element to an effective 3D hyperspectral capture system is an imaging device with adequate spatial and spectral resolution, reasonable capture times and well characterized accuracy and performance. While many published and commercial devices claim fast hyper- or multi-spectral capture, they are often limited to a small number (e.g., six) channels, or are designed for single scan line capture, where a spectral image is defined as spatial sample per column, and the image column data consists of spectral samples for that position. We turn to considering recently developed devices that show promise for our goal of a high spatial and spectral resolution camera that extends into both the UV and IR ranges.

Imaging Spectroscopy Techniques for discriminating spectral frequency can be classified as either bandpass- or dispersion-based imaging. Bandpass-based spectroscopy contains a set of narrow-bandpass filters on a motorized wheel or a liquid crystal tunable filter [Ware et al. 2000; Sugiura et al. 2000; Attas et al. 2003; Rapantzikos and Balas 2005]. A monochromatic solid-state detector in the systems measures the filtered narrow-band spectra, where the spectral and spatial resolutions depend on the specifications of the filters and the sensor. Our target optical resolution is ~10nm as in commodity spectrometers. Current bandpass filters for multispectral imaging have a ~15nm bandwidth with a Gaussian transmission distribution and nonuniform bandwidths across the range. Liquid crystal tunable filters are not suitable as their transmittance rapidly decreases from 500nm and cannot transmit a spectrum under 400nm.

Dispersion-based spectroscopy uses a diffraction grating (or a prism) and a solid-state array to measure spectrum dispersed by the diffraction grating (as shown in Fig. 2). Dispersion-based imaging spectroscopy was introduced to measure a spatially-varying spectral pattern on a 2D surface [Brady 2008]. Imaging spectroscopy disperses spatially-varying radiance through a coded-aperture mask. The key idea is that spectral dispersion of the incident image is captured by a 2D monochromatic sensor, rather than a 1D sensor array in the classical spectroscopy architecture. However, the spectral dispersions of neighboring radiances are recorded with one dimensional overlaps. The individual spectral dispersion of each ray can be iteratively solved from the overlaps by accounting for known spatial constraints of the coded aperture. Imaging spectroscopy is broadly used in many applications, including environmental remote sensing, military, astrophysics, and biomedical imaging.

Wagadarikar et al. [2008; 2009] introduced a single disperser architecture that can capture low resolution multispectral images up to 30 frames per second; the Du et al. [2009] system utilizes a prism instead of a diffracting grating. However, these dispersion-based imagers struggle with computational artifacts and present physical limits in resolving spectral discrimination. There are several approaches to overcome the tradeoffs between spectral and spatial resolution. Kawakami et al. [2011] appends an additional high-resolution trichromatic camera on the dispersion-based imager to estimate high-resolution multispectral information, assuming low frequency nature of reflectance of general objects. Kittle et al. [2010] introduce an approach to enhance spatial resolution by adding more multi-frame translations of the coded aperture as input. Recently, Habel et al. [2012] introduced a low-cost dispersion-based approach by using a commodity RGB camera, which achieves high spatial and spectral resolution within the human visible spectral range.

The spectral resolution of the bandpass-based imagers is coarser than dispersion-based imagers. But dispersion-based imagers require extensive processing time and suffer from computational artifacts. Although these systems provide a higher spectral resolution than the bandpass-based imagers, the spatial resolution is insufficient to capture high frequency surface patterns in 3D. There are some commercially available pushbroom cameras as employed in [Brusco et al. 2006]. Pushbroom-based imagers can provide higher-resolution multispectral images than the dispersion-based ones; however, the vertical resolution of the pushbroom cameras is five times lower than the horizontal one. Both resolutions are still lower than those of commodity cameras [Qin 2010]. The acquisition time also is significantly longer than the dispersion-based imagers and is not practical for high-resolution 3D scanning. For instance, the pushbroom camera takes an hour to capture a shot in the same target spectral range as ours, albeit at a lower spatial resolution. Our system achieves higher spatial resolution without sacrificing spectral resolution.

We build on Kittle et al.'s [2010] approach, but take advantage of both bandpass- and dispersion-based imaging. We further improve the computational post-processing required for this approach.

3 The Hyperspectral Imager

The image input in our system follows the dispersion-based compressive sensing systems [Wagadarikar et al. 2009; Du et al. 2009; Kittle et al. 2010] for efficient measurement. We begin by describing the basis of compressive sensing, the Kittle et al. system, and explain our modifications to this system. We detail the calibration of the system, and present the characterization of the system's performance.

3.1 Imager Configuration

Compressive Sensing Compressive sensing recovers accurate signals from samples significantly below the Nyquist rate under certain conditions, though these conditions are difficult to verify in practice since verification poses an NP-hard problem. We couple dispersive prism optics and a coded aperture mask to resolve spatio-spectral information for sampling. We then solve the under-determined system by solving sparsity-constrained optimization problems. Here we briefly describe our mathematical model that follows the single disperser design [Wagadarikar et al. 2009], to help understand the basic operations implemented by the optical elements. See Fig. 2 for an overview.

The output we want from the measuring system is the intensity of light f from a object as a function of wavelength λ at each physical location (x, y). The spectral density is relayed to the coded aperture plane through an objective lens as $f_0(x, y, \lambda)$. The spectral density is filtered by the random transmission function $T(x, y)$ printed on the aperture. The spectral density f_1 after the mask becomes

$$f_1(x, y, \lambda) = f_0(x, y, \lambda) T(x, y). \tag{1}$$

This coded spectral density is propagated through the relay optics and the dispersive element. Our prism unit disperses the spectrum along a horizontal axis. The spectral density after the dispersive unit can be described as propagation through unity linear dispersion α of wavelength λ from center wavelength λ_c, denoted as $\phi(\lambda) = \alpha(\lambda - \lambda_c)$. The density after the prism $f_2(x, y, \lambda)$ is

$$f_2(x, y, \lambda) = \iint h(x' - \phi(\lambda), x, y', y, \lambda) f_1(x', y', \lambda) dx' dy', \tag{2}$$

where the function h is the product of the Dirac delta functions of x and y axes, $\delta(x' - [x + \phi(\lambda)]) \delta(y' - y)$. However, the monochromatic detector array only measures the intensity of incident energy, insensible to the spectral density. Assuming the spectral response of the detector is flat, the captured spectral density on the detector $g(x, y)$ in a spectral range Λ is $\int_\Lambda f_2(x, y, \lambda) d\lambda$, an integral over the wavelength dimension of continuous dispersion with a mask modulation. (Wavelength-dependent attenuation, e.g., absorption in the lenses and quantum efficiency in the detector, is characterized later in Sec 3.3.) We then describe $g(x, y)$ as

$$g(x, y) = \int_\Lambda \iint h(x' - \phi(\lambda), x, y', y, \lambda) f_0(x', y', \lambda) T(x', y') dx' dy' d\lambda. \tag{3}$$

The detector pixelates the spectral density with pixel size Δ, where each pixel location (m, n) at image g corresponds to the physical location (x, y). The captured image $g(m, n)$ can then be described as

$$g(m, n) = \iint g(x, y) \text{rect}(\frac{x}{\Delta} - m, \frac{y}{\Delta} - n) dx dy. \tag{4}$$
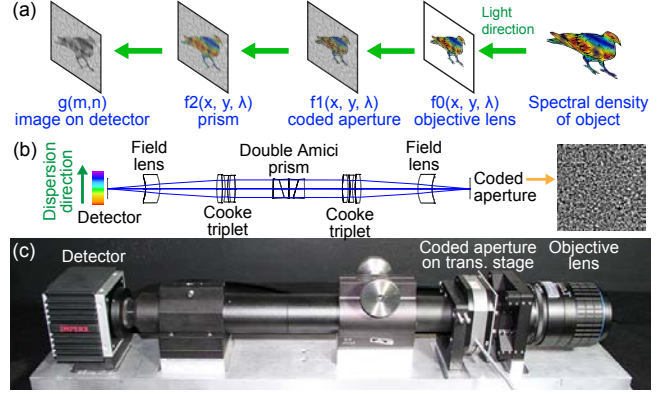

Figure 2: *Image (a) shows a schematic diagram of compressive sensing. Image (b) represents the optical paths from the coded aperture (right) to the detector (left). Inset (b): a snapshot of the coded aperture with a monochromatic light (bandwidth: 10nm from 560–570nm). Image (c) shows a photograph of our 2D imaging unit.*

Since each element of the coded aperture has the same size as that of a detector pixel Δ, the mask function $T(x, y)$ can be represented as a discrete Boolean function of a 2D array of square pinholes $t(i, j)$:

$$T(x, y) = \sum_{i,j} t(i, j) \text{rect}(\frac{x}{\Delta} - i, \frac{y}{\Delta} - j). \tag{5}$$

By substituting $g(x, y)$ and $T(x, y)$ in Eq. (4) with Eqs. (3) and (5), we can describe the received signal as

$$\begin{aligned} g(m, n) &= \sum_{i,j} t(i, j) \int_\Lambda \iiiint \text{rect}(\frac{x'}{\Delta} - i, \frac{y'}{\Delta} - j) \text{rect}(\frac{x}{\Delta} - m, \frac{y}{\Delta} - n) \\ &\quad \times h(x' - \phi(\lambda), x, y', y, \lambda) f_0(x', y', \lambda) dx' dy' dx dy d\lambda \\ &= \sum_{i,j} t(i, j) \Omega(i, j, m, n). \end{aligned} \tag{6}$$

Here, as our system disperses spectrum only horizontally and the aperture maps to the detector 1:1, j is the same as n, so that this model can be simplified to $\sum_i t(i, n) \Omega(i, n, m)$. In addition, assuming the dispersion of the prism is approximately linear in the spectral range, we can describe this model as $\sum_i t(i, n) f(i, n, m + i)$ by defining $f(i, n, m)$, a discrete and sampled version of $\Omega(i, n, m)$, such that $f(i, n, m + i) = \Omega(i, n, m)$ (see [Wagadarikar et al. 2009] p. 8 for definition). Then, we can rewrite $g(m, n)$ as $\sum_k t(k - m, n) f(k - m, n, k)$ by noting $m + i = k$, where k is discrete wavelength. This can also be written as a matrix-vector equation:

$$\mathbf{g} = \mathbf{H}\mathbf{f}, \tag{7}$$

where $\mathbf{H}$ is a non-negative and binary matrix. The matrix $\mathbf{H}$ is built by registering the mask pattern of the target wavelength following the dispersion coefficient. The matrix $\mathbf{H}$ projects voxels of the three-dimensional sampled and sheared information $\mathbf{f}$ to pixels of the detector array $\mathbf{g}$. By minimizing $||\mathbf{g} - \mathbf{H}\mathbf{f}||_2^2$, we estimate $\mathbf{f}$ as a hyperspectral image of the object.

Enhanced Spatial/Spectral Frequency The modulation transfer function (MTF), the amplitude ratio of output to input frequency, has been popularly used for evaluating the resolving power of imaging systems [Burns 2002]. According to the Nyquist theorem, a perfect system produces $p/2$ cycles per picture width p. The spatial frequency, where the MTF is 50% of its peak value, is called MTF50; this is a common performance metric for imaging systems. The spatial frequency responses of current dispersion-based imaging

systems are severely limited (aver. MTF50: 0.10–0.15) [Brusco et al. 2006; Wagadarikar et al. 2008; Du et al. 2009; Kittle et al. 2010], as compared to that of commodity RGB cameras (aver. MTF50: 0.20–0.35). Current *one-shot* dispersion-based systems are insufficient to reconstruct 3D hyperspectral patterns in practical applications and the number of pixels of these systems is typically less than 1M pixels.

To increase resolution, Kittle et al. proposed capturing S random translations of the mask. In Eq. (7), $\mathbf{g}$ and $\mathbf{H}$ are substituted with $[\mathbf{g}_1, \mathbf{g}_2, \ldots, \mathbf{g}_S]^\top$ and $[\mathbf{H}_1, \mathbf{H}_2, \ldots, \mathbf{H}_S]^\top$ respectively. Once we measure the linear translation of the projected dispersion $\mathbf{g}$, we calculate a hyperspectral image $\mathbf{f}$ by minimizing the objective function $O(\mathbf{f})$:

$$O(\mathbf{f}) = \frac{1}{2}\|\mathbf{g} - \mathbf{H}\mathbf{f}\|_2^2 + \tau\Gamma(\mathbf{f}), \qquad (8)$$

where $\Gamma(\mathbf{f}) = \sum_k \sum_{m,n} \sqrt{(f(m+1,n,k) - f(m,n,k))^2 + (f(m,n+1,k) - f(m,n,k))^2}$ (the total variation), and τ is a weighting parameter. In the initial iteration of $\Gamma(\mathbf{f})$, $\mathbf{f}$ is set to $\mathbf{H}^\top \mathbf{g}$ for regularizing sparsity [Chambolle 2004]. We solve the under-determined system by solving sparsity-constrained optimization problems $O(\mathbf{f})$ by using the two-step iterative shrinkage/thresholding (TWIST) algorithm [Bioucas-Dias and Figueiredo 2007]. We tested four methods, including GPSR [Figueiredo et al. 2007], NeARest [Sun and Pitsianis 2008], and SpaRSA [Wright et al. 2009]. We chose TWIST because it is the most efficient and accurate.

Overcoming Computational Intractability We aim to compute four megapixel resolution (2048×2048) with enhanced spatial frequency response, targeting MTF50 = ∼0.30, covering a NUV/VIS/NIR spectral range. Even though the translation architecture enhances spatial frequency, the optical design requires a significant amount of memory to solve Eq. (8). The resolution of Kittle's system is still limited spatially (640×480 pixels) and spectrally (450–650nm) because of the significant memory requirement. Therefore, we enhance the spatial/spectral frequency of the system by introducing a redesigned optical/computational structure.

Considering the aim of our system, our specification requires 55 translations and 53 target channels, each stored in single-precision float. The memory size of the matrix $\mathbf{H}$ in Eq. (8) is more than 50 gigabytes, exceeding the available memory in commodity computers.

Our design overcomes memory limitations without compromising spectral resolving power with two insights: (1) breaking the target spectrum into several bands and (2) parallelizing the computations. First, our method is based on the simple notion that bandpass filtered light can yield higher reconstructed spectral resolution [Wagadarikar et al. 2008; Du et al. 2009; Kittle et al. 2010]. By extension, our method filters the entire spectral range with a set of continuous bandpass filters and processes the dispersion of each band respectively. Three bandpass filters are placed sequentially in front of the objective lens to divide the detected spectrum (359nm to 1μm) into three bands (200-300nm) with minor overlaps. Since the incident light is bandpass filtered, the dispersed beam is narrower, and the detected light is linearly dispersed across a smaller fraction of the sensor width. The accumulated exposure at each pixel on the sensor includes fewer spectral dispersion overlaps of neighboring wavelengths of a given point on the viewed object, and the reconstructed spectrum for each image pixel is significantly improved. In addition, this design reduces the size of the matrices in Eq. (8). Fig. 7 compares the resolution improvement under various settings.

Second, we observe that the double Amici prism disperses the spectrum along a horizontal axis, so we can segment the original detector signals into several horizontal strips. Strip height is determined with respect to the maximum Y translation of the coded aperture in image

space. The strips are fed to the processor in the solution pipeline. We remove the upper and lower bounds of the strips which contain artifacts due to the translation of the coded aperture. Once individual computations are completed, the segments are stitched to complete the entire image.

3.2 Technical Specifications

Our 3DIS system measures continuous 3D hyperspectral patterns from NUV-A (359nm) to NIR (1μm), addressing the spectral characteristics of target specimens. Our system has been built with specialized optics that are apochromatic in the spectral range and exceed the spectral range of traditional imaging systems, where UV transmittance decreases rapidly due to absorption effects (below 400nm). In contrast to the IR band, the UV band is challenging for imaging due to the inherent transmittance characteristics of the optical substrate.

In our system, a random-pattern coded aperture is lithographically etched on a quartz substrate with an active area of 14.71mm square. A Newport X–Y piezo translation stage modulates the aperture by 160μm travel per axis or 21 pixels on the detector. The aperture code is 1:1 mapped onto the Imperx (w/o microlenses) 2048×2048 pixel, 15.15mm square, monochromatic detector (7.4μm pixel pitch). The internal optical design includes relay lenses and a double Amici prism (See Fig. 2(b)). The prism is made of fused silica (FS) and calcium fluoride (CaF_2). The field lenses are made of FS. The Cooke triplets are made of CaF_2 and BK7. A Coastal Optics 60mm f/4 UV-VIS-IR lens that is apochromatic from approximately 315nm to 1.1μm is mounted to our imager. Three bandpass filters, placed in front of the objective lens, narrow the incident spectrum measured by the detector. Fig. 3(a) qualitatively compares the quantum efficiency of the detector to the transmittance of each bandpass filter: (a) 351–527nm, (b) 514–709nm, and (c) 663nm–1μm.

For measuring hyperspectral reflectance, we employ a Xenon light source (oxygen-free Osram XBO 75W), which emits a mostly flat spectrum from 350nm to more than 1μm. See Fig. 4(c) for spectrum. We customize a lamp housing in order to uniformly illuminate the object surface. We mount a plano-concave lens in front of the light source to remove the shadow cased by the bulb socket in the light housing structure. Finally, we attach a UV-transmitting diffusion filter (10cm^2). The angle between the imager and the light source axes is 7.39° in order to avoid mirror reflection, following the design of laboratory spectroradiometers of 0/8 measurement geometry [Battle 1997]. Instead of multiple light sources, we use a single light configuration for illumination [Levoy et al. 2000]. The illumination is calibrated with a white standard reference, Spectralon, of which reflectance is known and optically flat to 99% from 250nm–2.5μm [Labshpere 2011].

For measuring UV fluorescence, we use a Spectroline Ultraviolet Transilluminator, which emits NUV-A & B. See Fig. 4 (c) for spectrum. We carefully design the UV incident light spectrum so that our
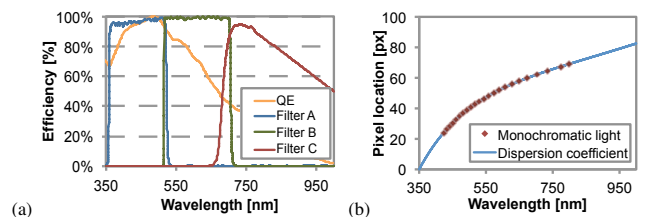

(a) (b)

Figure 3: *Plot (a) shows our three bandpass filters, as compared to the detector's quantum efficiency (QE). The filters' bandwidths are 200–300nm with minor overlap, and they are placed in front of the objective lens. (b) Relative pixel location of dispersion coefficient.*

fluorescent measurements are not contaminated by direct reflectance of the incident energy from the surface. This allows us to achieve a good signal-to-noise ratio within the VIS/NIR spectrum. Note that we treat the spectral wavelength under 380nm for UV fluorescence measurement separately because it overlaps the spectral range of the UV light and the imager.

3.3 Characterization

Dispersive Calibration We calibrate the non-uniform spectral distortion of our system. As the wavelength increases, the image of the aperture code shifts from right to left due to dispersion by the double Amici prism. The projected spectrum is non-uniformly distributed on the image plane with respect to wavelength [Wagadarikar et al. 2008; Du et al. 2009]. We calibrated the optical dispersion with 23 monochromatic light sources by using a grating monochromator. See Fig. 3(b). An incident ray with a spectrum from 359nm to 1,003nm disperses over 80 pixels, an average optical resolution of 8.06nm per pixel. The dispersion shift changes non-linearly. The short wavelength (Filter A: 351-527nm) shifts more than the longer one, and has a finer optical resolution (3.49nm) than the other two. We therefore subsampled wavelengths of this filter band (in 1/3) to balance its spectral resolution with those of the others. Overall, the optical resolution is 12.37nm with a std. dev. of 4.75nm. A nonlinear least squares fitting of the 23 samples captures the dispersion coefficient for the double Amici prism. This function is used to build matrix **H** in Eq. (7) from a captured coded aperture mask at a wavelength, 560nm.

Radiometric Calibration We employ a set of radiometric measurements of training colors—a white reference Spectralon and 240 color patches (Fig. 4(a))—to characterize the spectral response f_λ of our system for a given incident radiance $L_{r,\lambda}$. We determine a linear mapping P_λ, which describes $Q_\lambda^{-1} T_\lambda^{-1} F_{A,B,C,\lambda}^{-1}$ in the following manner:

$$f_\lambda = Q_\lambda T_\lambda F_{A,B,C,\lambda} L_{r,\lambda}, \tag{9}$$

where Q_λ is the quantum efficiency of the detector at each wavelength λ; T_λ is the internal scattering and transmittance of the optical system; $F_{A,B,C,\lambda}$ is the transmittance of the three bandpass filters. Based on training data, a constant scale factor for each wavelength P_λ is fit through the use of least squares learning. Note that the raw signal linearly corresponds to the incident spectrum (Fig. 4(d)). The radiometric calibration allows us to estimate the actual incident radiance value $L_{r,\lambda}$ after computationally solving **f** in Eq. (8).

3.4 Radiometric Accuracy and Spatial Frequency

Radiometric Accuracy We compared the accuracy of spectral reflectance measurements of our 3DIS system, as compared with typical imaging devices: a trichromatic camera (Nikon D100) and a five-channel hyperspectral camera (QSI 583WS). We employed a calibrated hyperspectral spectroradiometer (OceanOptics USB 2000) for radiometric measurements. Fig. 6(a) compares the hyperspectral reflectances of red, green, and blue color patches measured by the spectroradiometer and our 3DIS system (see Fig. 5 for the test color sample). The reflectances measured by these two instruments strongly correlate over all wavelengths. The light orange section in the plot indicates the human visible spectrum (400–700nm). It is worth noting that we evaluate our system performance across the hyperspectral spectrum (from 359nm to 1μm) that greatly exceeds the human visible spectrum. Therefore, we quantitatively compare the coefficient of determination and the median relative differences between the systems and the spectroradiometer across NUV/VIS/NIR. Fig. 6(b) quantitatively compares the overall radiometric accuracy
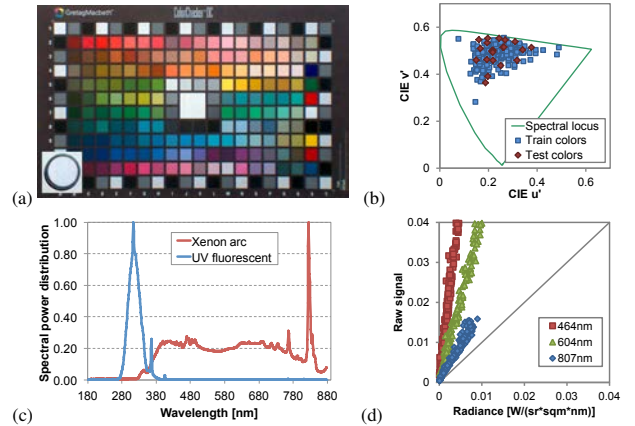

Figure 4: *(a) Training colors for radiometric calibration, captured by our system. The spectra of the colors distribute broadly from 359nm to 1μm (GretagMacbeth DC chart and Spectralon (inset) under a Xenon light source). (b) The color gamut of training/test color samples. (c) Spectral power distributions as a function of the wavelength emission of the Xenon arc and UV fluorescent bulbs. (d) An example of raw signal distributions as function of the incident radiances from 241 colors at 464, 604, and 807nm.*

of the three systems on 25 color patches (Spectralon and 24 color patches). The radiometric measurements of our 3DIS system achieve greater accuracy as compared to reference systems.

We also computed the well-known color differences CIE ΔE_{00} of the test color measurements w.r.t. human color perception (400–700nm) [CIE 2001]. The median ΔE_{00} of three systems are 14.71 (Nikon), 16.06 (QSI), and 7.15 (3DIS) with std. devs. of 4.92 (Nikon), 6.31 (QSI), and 1.56 (3DIS) respectively. The accuracy of our system significantly outperforms the reference systems even in the human visible spectrum.

Spatial Frequency Our implementation of imaging spectroscopy enhances spatial frequency response (SFR) by employing bandpass filters, dispersive elements and parallelized computation, while simultaneously enhancing spectral resolution and range. A spatial frequency measurement chart, ISO 12233 [ISO 2000], was captured to evaluate SFRs of our 3DIS system and two reference imaging systems: the Nikon and the QSI cameras (Fig. 7(f)). The horizontal and vertical SFR of our hyperspectral imaging system rivals that of a commodity RGB camera, sufficient for high-resolution hyperspectral 3D measurements of small-sized objects (Nazca cup: 9.76cm tall, shown in Fig. 12). The horizontal SFR (along the spectral dispersion axis) exceeds the vertical SFR due to the image reconstruction algorithm described in Sec. 3.1. Note that the commodity RGB camera captures the highest spatial resolution.

In Fig. 7, the horizontal/vertical MTF50 values (higher value is better) of the commodity Nikon camera is 0.31–0.35; the MTF50 values of the bandpass-based hyperspectral camera are about 0.20. The MTF50 of our 3DIS system rivals that of the commodity RGB camera (0.27–0.35) but in addition, our system provides an 18 times higher spectral resolution, as compared to the RGB camera. The spatial frequency outperforms other commercial dispersion-based imager [Brusco et al. 2006]; this particular system was therefore limited to investigating architectural-scale color changes. The right plot shows the measured spatial frequency response at 523nm for our 3DIS system.

The translation architecture enhances spatial, not spectral, frequency. Using translation achieves a higher resolution on given optical features. In addition, spatial frequency has a significant indirect effect
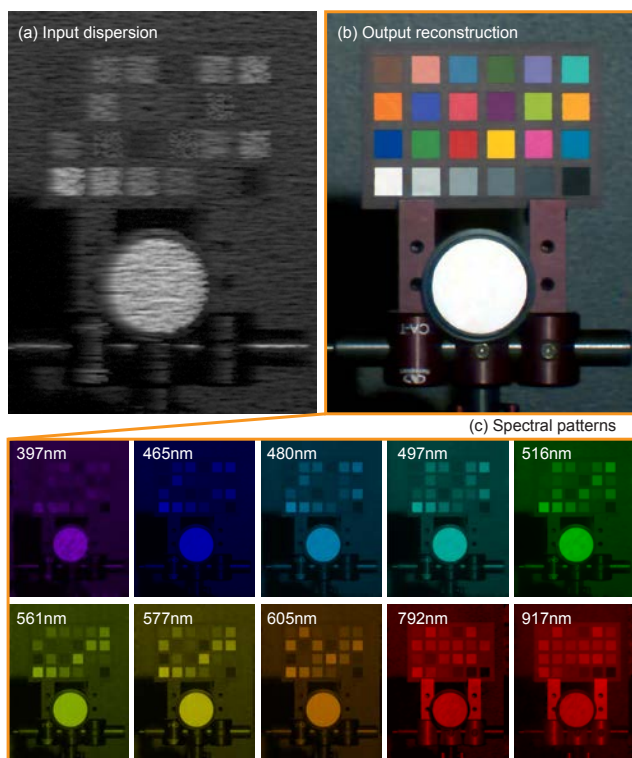
Figure 5: *(a) Input dispersion at a single position of the coded aperture, captured by the monochromatic detector. (b) Final color visualization output, adjusted for human color perception. (c) Spectral reconstruction output: ten of 53 discrete wavelengths from 359nm to 1μm in ~12nm intervals. The invisible spectral wavelengths of 397, 792, and 917nm are represented in pseudo-colors.*
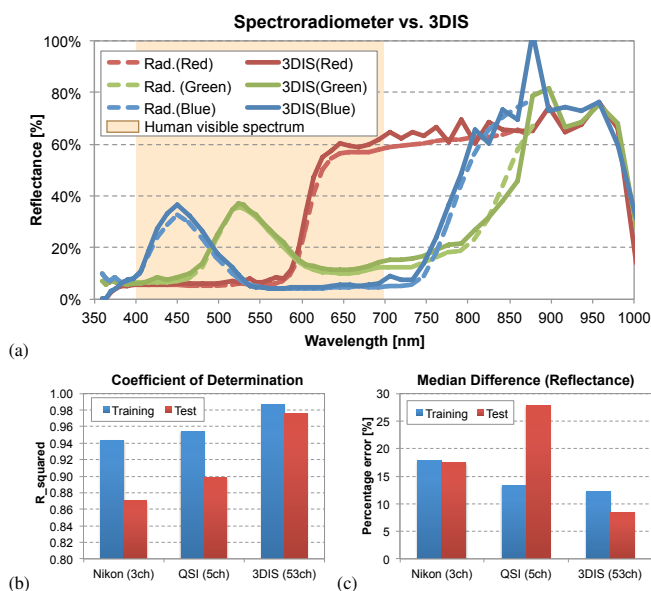

Figure 6: *Plot (a) presents hyperspectral reflectances of red, green, and blue test color patches (see Fig. 5) measured by our 3DIS system and a spectroradiometer. The light orange section in the plot indicates the human visible spectral range of 400–700nm. Plot (b) quantitatively compares the radiometric accuracy of three imaging spectroscopies: a trichromatic Nikon camera, a five-channel hyperspectral camera, and our 3DIS system. The spectral measurements of our system are significantly more accurate.*
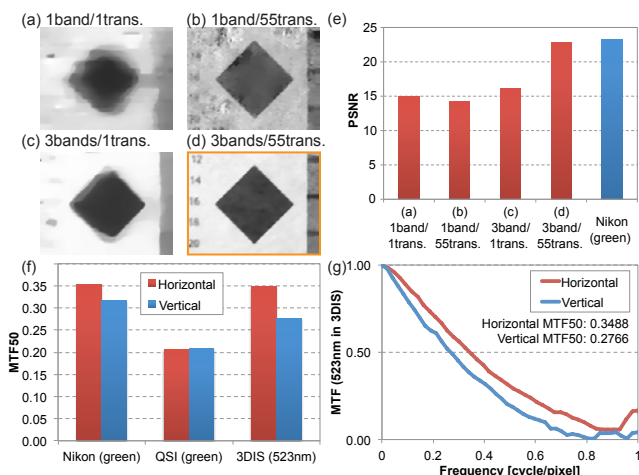

Figure 7: *Images (a)-(d) present the reconstructed spectral pattern at 523nm from four different optical designs: (a) a single broadband input (359nm–1μm) without any translation of the coded aperture, (b) the same spectral input as (a) with 55 translations of the aperture, (c) three bandpass input without any aperture translation, and (d) our chosen image reconstruction method: three bandpass input with 55 translations of the coded aperture. Plot (e) presents peak signal-to-noise ratio (PSNR) of the four optical designs, as compared to Nikon camera. Plot (f) compares the spatial frequency response of our 3DIS system against two reference imaging systems: the Nikon and the QSI cameras. Plot (g) shows horizontal/vertical MTF functions of our 3DIS system.*

on spectral accuracy. Poorly reconstructed spectral channels (where each pixel represents radiometric intensity of the surface point) contain smoothed edges and random noise. See Fig. 7(e) for measured peak signal-to-noise ratios. In our system, point-to-point readings of each spectral map yield spectral accuracy.

4 3D System Integration

We integrate the hyperspectral imager described in the previous section into a system for 3D shape and reflectance measurement. Fig. 1 provides an overview of our system.

Hardware Setup and Calibration We use a classic strategy similar to the one presented in [Farouk et al. 2003]. We mount the imager, a laser scanning system and Xenon light source on a standard optical table, located in a black walled room. A diagram and photograph of the setup are shown in Fig. 8. The scanner is a ShapeGrabber dual slit laser range scanner, based on the BIRIS technology from NRC Canada [Elgazzar et al. 1997]. This scanner is chosen for its high sensitivity to low signals on dark surfaces. The depth accuracy of the scanner is 0.1 mm, while its horizontal and vertical resolution is 0.5–1mm. A motor controlled turntable (Kaidan MDT-19) is used to spin the object around a vertical axis, exposing each viewpoint to the laser scanner and hyperspectral imager. The positions of the imager system, light source and turntable axis are calibrated in terms of the laser scanner coordinate system, using standard calibration targets shown in Fig. 9. Capturing the reference target specifically allows us to determine the geometric relationship between the range scanner and the imager. The calibration error mapped in the image plane has a mean of 1.036 pixels and a std. dev. of 0.66; the calibration error mapped to the object space has a mean of 0.198mm and a std. dev. of 0.124.

Reflectance Estimation Using the laser scan and image data registered into common coordinates, the diffuse reflectance is estimated

for the spectral range of wavelengths using the measured reflected radiance $L_{r,\lambda}$ from the imager calibrated for non-linear response:

$$L_{r,\lambda} = \rho_\lambda E_{i,\lambda} \cos \theta_i. \qquad (10)$$

where $E_{i,\lambda}$ is the incident light energy and θ_i is the angle between the surface normal and the light source. The quantity of incident light on the surface varies with the squared distance d^2 between the Xenon light source $L_{i,\lambda}$ and the surface:

$$L_{r,\lambda} = \rho_\lambda L_{i,\lambda} \cos \theta_i / d^2. \qquad (11)$$

It is worth noting that Eqs. (10) and (11) hold for the entire wavelength band λ. A reference value of $L_{i,\lambda}$ for the light source is estimated by imaging the diffuse and flat white target with known reflectance. Since the values of θ_i and d are known for each point from the scanned geometry, the value of $L_{r,\lambda}$ is all that is needed to solve for the reflectance ρ_λ at a point. We merge the individual scans mapped with reflectance measurements into a single unified representation for each object, making use of MeshLab [3DCoForm 2012] for scan alignment and mesh integration. We partition the mesh into non-overlapping parts, and project and combine the individual maps of reflectance data onto the partitions, in a method similar to [Bernardini et al. 2001]. This produces a seamless map of reflectances across the entire object. An improved value is obtained as multiple views are captured from different orientations of the object, and a weighted average value is found for ρ_λ. To avoid specular highlights affecting the calculation, incident and reflected direction pairs that are near mirror reflection are excluded from the calculation.

Performance Acquiring the hyperspectral reflectance of one object from 16 different viewpoints takes 8 hours (12 hours for UV-induced fluorescence). The 1/2 hour per view is needed to cycle through the three filter bands, and then take exposures for multiple coded aperture positions. For a typical compact object (such as a bird specimen) we capture 16 views using 45-degree intervals and two different orientations. Currently, we use unoptimized code for the reconstruction. Most of the computational time is used for reconstructing the hyperspectral information. Reconstructing 53 discrete spectral channels from each bandpass channel at each camera view takes about two hours on an eight-core 3GHz Xeon processor with 32GB RAM. We compute each patch in parallel by distributing computations to available machines and cores. Within each calculation, we make use of multicores through multithreaded LAPACK. Then, reconstructing the geometry and hyperspectral texture maps takes about 11 hours (may vary depending on the geometric complexity and size of the object). Total acquisition and processing time is approximately 96 hours per 3D object, processed in parallel. The GPU-based code optimization for the reconstruction pipeline is our future work.

Visualization Our system acquires two different types of measurements: hyperspectral reflectance (calculated by using the radiance of the object and reference white, 3D geometry, and light source) and UV fluorescence (same input, but without UV reflectance). These texture maps are packed as a multi-layer OpenEXR texture map. The reflectance is rendered by integrating the spectral products of reflectance and a virtual illumination; the fluorescence is rendered by integrating only fluorescence. We use a quasi-random path tracer that uses parametric quasi-Monte Carlo integration, iRay [nVidia 2012]. We can render each wavelength band as a gray scale image. Note our spectral measurement includes some modest inter-reflection and sub-surface scattering, which are diminished by scanning and averaging over multiple views. Alternatively we can project the hyperspectral rendered images into the appropriate basis for the vision system we wish to simulate – e.g., trichromatic values for humans [Vos 1978], or four channels for a bird species [Stoddard and Prum 2008].
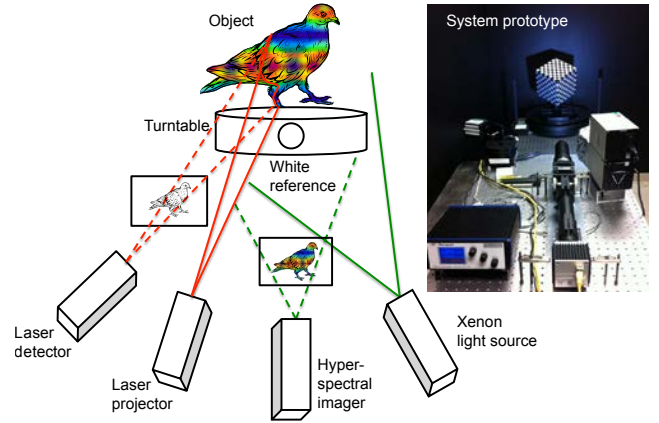

Figure 8: *Principles of our 3DIS system for measuring reflectance. A laser projector shines a thin sheet of light onto the object. The laser sensor detects, on each scan line, the reflected laser light to produce a depth map. A Xenon light source illuminates the surface with a broad spectrum. Our hyperspectral imager measures reflected radiance to compute a reflectance map with respect to reference white. Inset: a photograph of our prototype system.*
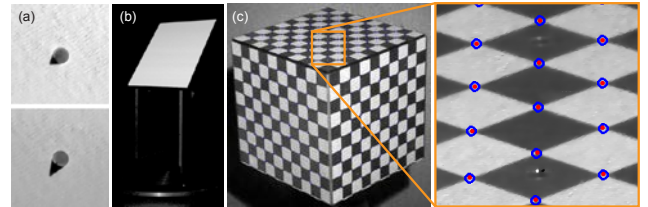

Figure 9: *(a) Shadows from two conical pins on the light vector calibration target, captured by our hyperspectral imager. (b) The turntable calibration target. (c) The geometric calibration target, captured by our imager. Closeup: qualitative comparison of the registration accuracy. The blue circles show the ground truth on the reference 3D cube; the red dots indicate the predicted mapping of object coordinates on the image plane.*

5 Results

We demonstrate practical and scientific applications of our 3DIS system for measuring hyperspectral patterns on 3D objects. In collaboration with the department of Yale Ecology and Evolutionary Biology, and in association with the Yale Peabody Museum of Natural History, we deployed our system to non-destructively study 3D reflectance and fluorescence patterns of biological organisms, minerals and an archaeological artifact. For visualizations of these 3D spectral patterns, refer to the supplementary video.

5.1 Ornithology

Vision Many organisms have evolved visual capacities that exceed that of humans, e.g., wide field of view, increased retinal resolution, carotenoid filters to cones to increase wavelength resolution, more than three color channels, and expanded spectral sensitivity. In the case of birds, visual sensitivity extends from NUV to red [Chen and Goldsmith 1986; Hart 2001]. In addition to three color cones with spectral sensitivity similar to that of the human visual system, birds have a fourth avian opsin with sensitivity in the NUV spectrum [Chen et al. 1984; Hart 2001]. This fourth opsin appears as either violet wavelength sensitive (VS) with a peak between 400–410nm, or as ultraviolet sensitive (UVS) with peak sensitivity
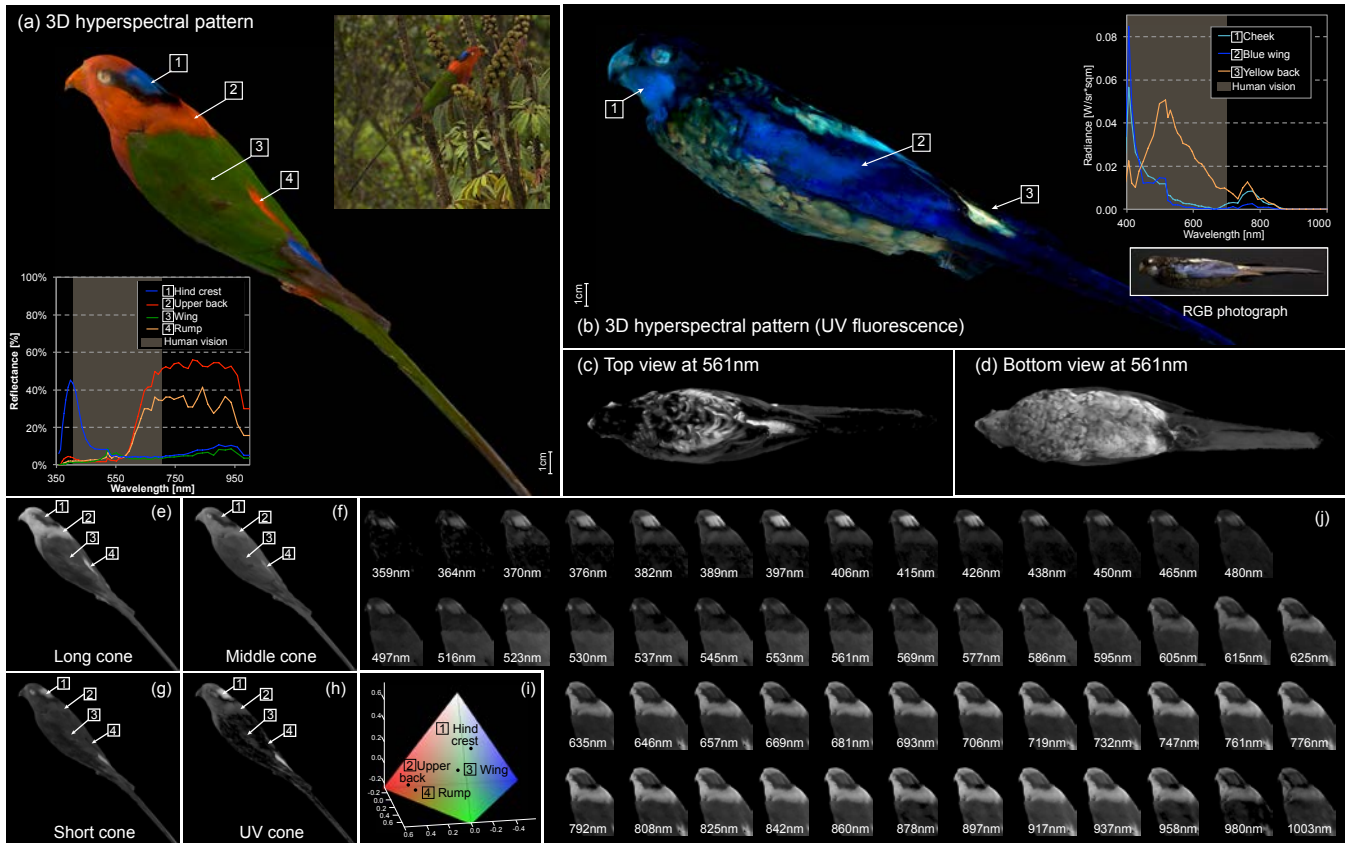
Figure 10: *(a)* Charmosyna papou goliathina*, Papuan Lorikeet (Yale Peabody Museum: YPM41702): Hyperspectral reflectance and tetrachromatic color of the blue of the hind-crown, red of the upper back, green of the lower back, and red of the rump. Inset (top): simulation rendering of the bird in its natural environment. Inset (bottom): diffuse reflectance readings (359nm–1μm) on the 3D hyperspectral patterns as compared to human vision. (b)–(d) UV-induced visible-fluorescence of the plumage of* Platycercus venustus*, Northern Rosella (Yale Peabody Museum: YPM74652): yellow fluorescing contour feathers of the back and belly. Blue fluorescing wing feathers, and contour feathers of the crown and cheek. Inset: radiant emission readings of UV-induced fluorescence. (e)–(h) Each represents the photon catch on* C. papou goliathina *of one of the tetrachromatic cones: U, S, M, and L. (i) Three-dimensional chromaticity representation of the plumage of the bird in the USML tetrahedron color space [Stoddard and Prum 2008]. (j) The entire hyperspectral patterns of the bird in 3D. Refer to the supplementary video for visualizations of full 3D spectrum.*

between 350–375nm, but both have extensive absorbance down into the near UV. Humans have inherited the degenerate color system of primitive mammals, which lost UV sensitivity millions of years ago. Our system can compensate for the limits of human color vision, simulating what birds see with their enhanced color vision (Fig. 10).

To represent the chromaticity space of avian vision, we project the four-dimensional *tetrastimulus* space into the three-dimensional space of a regular tetrahedron (or simplex) [Stoddard and Prum 2008]. See Fig. 10(i). The base of the tetrahedron represents the 2D chromaticity derived from the long, medium, and short wavelength receptors alone. The peak of the tetrahedron adds the third chromaticity dimension derived from either the VS or UVS sensitive cone type. The achromatic point (i.e., white, gray or black) is located at the weighted center of the tetrahedron. A given spectrum is represented as a single point in the tetrahedral color space and defined by a vector of three polar coordinates: hue (θ and ϕ) and chroma (radial distance from the achromatic point).

The implications of ultraviolet sensitivity to avian color vision has greater ramifications than simply extended spectral sensitivity. The additional spectral channel in the NUV provides a fourth color dimension. Consider the color purple which is not a pure spectral color, but a combination of red and blue, nonadjacent wavelengths in the visible spectrum. Birds see all the same colors as humans,

but they benefit from an expanded class of colors of non-adjacent wavelengths. Avian color space incorporates novel unimaginable colors, e.g., ultraviolet–red, ultraviolet–yellow, and ultraviolet–purple. White has a balanced amount of ultraviolet, and as such is redefined for birds.

Reflectance Color reflectance is a crucial component of the phenotype of many organisms. Organismal color reflectance can alternately function as camouflage or a visual form of communication within and among species [Land and Nilsson 2002]. The spectral reflectance of the color patches on the surface of an organism define its color phenotype. Documenting spatial variation in spectral reflectance, including UV, is essential to understanding the role of color in the choice of mates, dominance relationships, and reproductive success [Bennett et al. 1996].

Birds are the most colorful land vertebrates; almost every color imaginable and visible to humans can be found in the avian world [Stoddard and Prum 2011]. A single bird can display a startling range of hue across its plumage. Furthermore, avian plumage coloration mechanisms take advantage of avian UV spectral sensitivity widening the color gamut outside human visual sensitivity [Andersson et al. 1998]. The higher dimensional avian color gamut makes birds ideal test subjects for our 3D hyperspectral imaging spectroscopy.
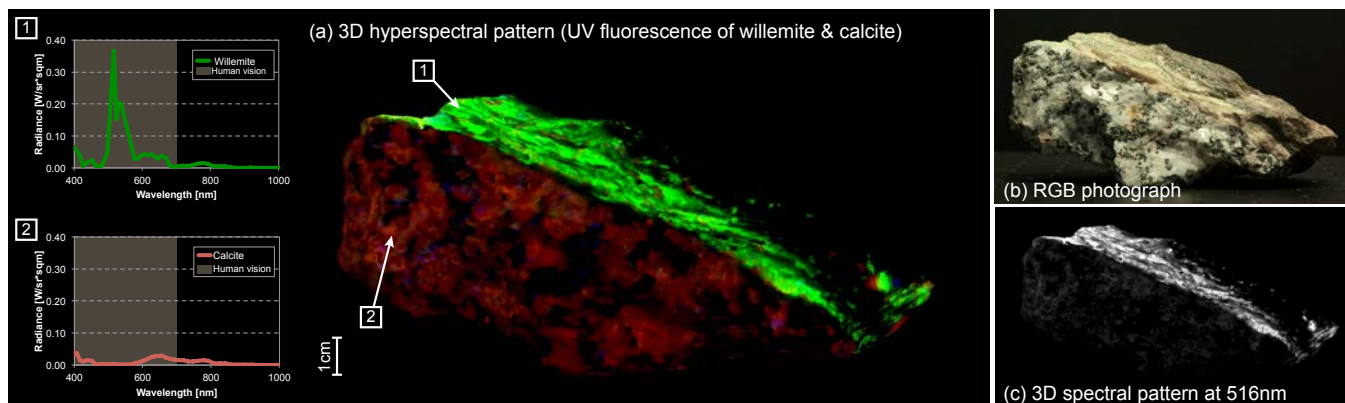
Figure 11: *Metamorphic ore containing willemite, calcite, and magnetite, Franklin Furnace, NJ (Yale Peabody Museum). (a) Rendered 3D hyperspectral pattern of UV fluorescence and associated spectra, as measured by our system: green fluorescence indicates willemite and red fluorescence indicates calcite. Inset (top): NUV-induced fluorescent radiance of willemite. Inset (bottom): fluorescent radiance of calcite. An ultra-violet spectrum (260–390nm) illuminates the object, and the emitted fluorescent radiance (excluding reflected UV) is measured and rendered in 3D. (b) Appearance of the ore under white light captured in a photograph. (c) Rendered 3D spectral pattern at 516nm, where the willemite presents a spectral peak of fluorescence.*
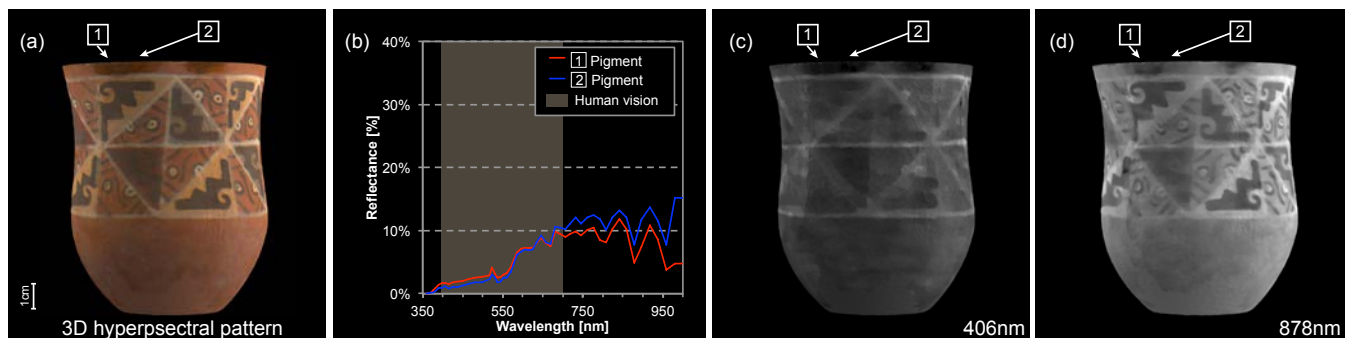

Figure 12: *Nazca cup, excavated in Nazca valley, Peru in 100 B.C.–600 A.D. (Yale Peabody Museum: ANT258589). Renders indicating efforts to restore the Nazca cup: (a) human visible color representation, (b) hyperspectral reflectance readings, compared to human visible spectrum, (c) & (d) compare rendered 3D hyperspectral patterns at 406nm and 878nm. Superficially the cup was restored by using a single material; however, a NIR reflectance at 878nm reveals two potentially different materials were introduced in past restoration.*

Figs. 10(a) and (e)–(j) show 3D renderings of *Charmosyna papou goliathina*, Papuan Lorikeet. In a study of 111 avian species, Papuan Lorikeet achieved one of the highest color volumes, which means that the avian eye senses dramatic color variation [Stoddard and Prum 2011]. The UV-blue reflectance of the hind-crown coupled with UV sensitivity of the avian eye increases the spectral bandwidth as compared to blue reflectance alone. This leads to increased signal to noise ratio and increases visibility in avian visual communication. The black band of the nape (near zero reflectance from NUV to NIR) is strategically placed directly behind the hind-crown, maximizing contrast of surrounding colors.

UV Fluorescence The application of fluorescence to the study of chemical composition of color pigments in plumage presents potential scientific opportunities for study [Mcgraw 2006]. A previous behavioral study has considered the role of UV-induced visible-fluorescence in the courtship display of *Melopsittacus undulatus*, Budgerigar [Arnold et al. 2002]. The additional chromatic signal contributed by UV-induced fluorescence of the yellow-colored plumage of the crown and cheek, as detected by the visual system of a potential mate, has been shown to play a role in sexual selection. Our system is an ideal complement to such behavioral studies, in that we measure both plumage hyperspectral reflectance as well as UV-induced fluorescence, then we map both on the surface geometry of the bird. Investigation of intra- and inter-species color variation can be performed from our 3D spectral patterns.

Figs. 10(b)–(d) contain 3D renderings illustrating the spectral emission of the UV-induced visible-fluorescence of *Platycercus venustus*, Northern Rosella. Figs. 10(c) and (d) show the yellow-green fluorescing contour feathers of the back and belly. Blue-fluorescing feathers of the crown, cheek, and wing are shown in Fig. 10(b).

5.2 Geology

Fluorescent minerals are prized for their dramatic color and surface patterns. Fluorescent color can be a useful guide to identify minerals randomly distributed in 3D space on the surface of a specimen. We can extract the estimated 3D locations of a target mineral from a collected ore sample. Fig. 11(a) shows the UV-induced fluorescent 3D pattern reconstruction of an ore sample containing willemite, calcite and magnetite. Fig. 11(c) selectively detects the 3D location of willemite in the mixed mineral. Our system identifies the willemite in this ore as belonging to the Franklin-Sterling Hill District, NJ by detecting its peak fluorescence at 516nm. Our measurement shows inter-instrumental agreement with a previous measurement of willemite in ore extracted from the Franklin-Sterling Hill District [Newsome and Modreski 1981]. Additionally, our system selectively detects the geometric distributions of calcite (reddish orange, a peak at 645nm) and magnetite (blueish black).

5.3 Cultural Heritage and Fine Arts Applications

In recent years the development of numerous non-invasive techniques for the documentation, investigation and conservation of objects of cultural heritage have been pursued. Various forms of spectroscopy (energy-dispersive, X-ray diffraction, X-ray fluorescence, ultraviolet-visible, Fourier-transform infrared, etc.) are applied in museum labs and conservation studios to identify pigments and varnishes, locate old repairs or damage, and reveal an artist's working process [Saunders and Cupitt 1993; Thoury et al. 2005; Fischer and Kakoulli 2006]. The majority of these techniques, including ultraviolet-induced fluorescence and multispectral imaging, have been conceived for and applied to 2D artworks, i.e., paintings and drawings [Thoury et al. 2005; Zhao et al. 2008]. Others have explored extending these functions into 3D [Brusco et al. 2006]. Our 3DIS system is capable of capturing hyperspectral datasets of *complete three-dimensional* cultural objects (polychromal sculpture, ceramics, etc) to assist archaeologists, art historians, and conservators in their study and preservation of objects of cultural value. Fig. 12 demonstrates 3D renderings of an excavated and restored Nazca cup (in Nazca valley, Peru in 100 B.C.–600 A.D.) evidencing two repaired regions near its rim.

6 Conclusion and Discussion

We have described a 3D scanning system that incorporates hyperspectral imaging to capture the reflectance of the entire surface of an object. Through the use of dispersion- and bandpass-based imaging, our system overcomes the tradeoffs between spectral and spatial resolutions in previous hyperspectral imaging systems. The accuracy and resolution of our system rival that of commodity spectrometers; our system can be viewed as a 3D version of a commodity laboratory spectrometer, resolving spectral patterns in 3D space with high accuracy at twice the spectral range. We demonstrate our system with applications in ornithology, geology and cultural heritage.

There are several areas for future work. In the case of UV-induced fluorescent measurements, our system quantizes the diffuse fluorescent emission from the object surface. The images of the fluorescent bird and mineral in Figs. 10 and 11 are rendered with a path-tracer [nVidia 2012], accounting for diffuse surface emission as purely Lambertian. Rendering spatially-varying subsurface scattering of the incident UV energy would be interesting future work.

The prototype version of our system achieves a spectral range from 359nm to 1μm. However, ornithologists researching the ecology and evolution of color ideally need to measure down to 300nm. The avian visual system is sensitive to UV spectral patterns between 300–400nm. Furthermore, avian integuments have evolved elaborate UV reflecting patterns as a function of sexual selection. Most of the optical substrates in our system (FS and CaF_2) transmit well below 300nm. However, the transmittance of borosilicate crown glass BK7, the optical substrate of the center element of each Cooke triplet, decreases rapidly below 350nm due to absorption effects. In future, the BK7 components will be replaced with an alternative substrate.

Our system modification made the acquisition and processing of high resolution spectral data possible. The processing is completely automatic, and data for a single object can be processed in parallel. However, the acquisition and processing times, while manageable, still limit the range of applications for the system. Future work includes both additional physical design and algorithmic improvements to reduce acquisition and processing time.

More generally, we would like to make our system sufficiently compact as to load the Xenon light source and the imager on a gantry, allowing us to measure iridescent and bi-directional reflectance.

Acknowledgements

References

3DCOFORM, 2012. MeshLab. http://meshlab.sourceforge.net/.

ANDERSSON, S., ORNBORG, J., AND ANDERSSON, M. 1998. Ultraviolet sexual dimorphism and assortative mating in blue tits. In *Proc. R. Soc. Lond.*, vol. 265, 445–450.

ARNOLD, K. E., OWENS, I. P. F., AND MARSHALL, N. J. 2002. Fluorescent signaling in parrots. *Science 295*, 5552, 92.

ATTAS, M., CLOUTIS, E., COLLINS, C., GOLTZ, D., MAJZELS, C., MANSFIELD, J., AND MANTSCH, H. 2003. Near-infrared spectroscopic imaging in art conservation: investigation of drawing constituents. *J. Cultural Heritage 4*, 2, 127–136.

BATTLE, D. R. 1997. The measurement of colour. In *Colour Physics for Industry*, R. McDonald, Ed., 2nd ed. Soc. Dyers Col., Bradford, 57–80.

BENNETT, A. T. D., CUTHILL, I. C., PARTRIDGE, J. C., AND MAIER, E. J. 1996. Ultraviolet vision and mate choice in zebra finches. *Nature 380*, 433–435.

BERNARDINI, F., AND RUSHMEIER, H. 2002. The 3D model acquisition pipeline. *Comput. Graph. Forum 21*, 2, 149–149.

BERNARDINI, F., MARTIN, I. M., AND RUSHMEIER, H. E. 2001. High-quality texture reconstruction from multiple scans. *IEEE Trans. Vis. Comput. Graph. 7*, 4, 318–332.

BIOUCAS-DIAS, J., AND FIGUEIREDO, M. 2007. A new twist: two-step iterative shrinkage/thresholding for image restoration. *IEEE Trans. Image Processing 16*, 12, 2992–3004.

BRADY, D. J. 2008. *Optical Imaging and Spectroscopy*. Wiley-interscience, New Jersey.

BRUSCO, N., CAPELETO, S., FEDEL, M., PAVIOTTI, A., PO-LETTO, L., CORTELAZZO, G. M., AND TONDELLO, G. 2006. A system for 3D modeling frescoed historical buildings with multispectral texture information. *Machine Vision and Appl. 17*, 6, 373–393.

BURNS, P. D. 2002. Slanted-edge MTF for digital camera and scanner analysis. In *Proc. PICS Conf.*, IS&T, 135–138.

CHAMBOLLE, A. 2004. An algorithm for total variation minimization and applications. *J. Mathematical Imaging and Vision 20*, 1–2, 89–97.

CHEN, D. M., AND GOLDSMITH, T. H. 1986. Four spectral classes of cone in the retinas of birds. *J. Comparative Physiology A 159*, 4, 473–479.

CHEN, D. M., COLLINS, J. S., AND GOLDSMITH, T. H. 1984. The ultraviolet receptor of bird retinas. *Science 225*, 4659, 337–340.

CIE. 2001. Improvement to industrial colour difference equation. CIE Pub. 142, Commission Internationale de l'Eclairage, Vienna.

DEVLIN, K., CHALMERS, A., WILKIE, A., AND PURGATHOFER, W. 2002. Tone reproduction and physically based spectral rendering. *Eurographics 2002: State of the Art Reports*, 101–123.

DU, H., TONG, X., CAO, X., AND LIN, S. 2009. A prism-based system for multispectral video acquisition. In *Proc. Int. Conf. Comput. Vision (ICCV)*, IEEE, 175–182.

ELGAZZAR, S., LISCANO, R., BLAIS, F., AND MILES, A. 1997. 3-D data acquisition for indoor environment modeling using a compact active range sensor. In *Proc. the IEEE Instrumentation, Measurement and Technology Conference*, 1–8.

FAROUK, M., RIFAI, I. E., TAYAR, S. E., SHISHINY, H. E., HOSNY, M., RAYES, M. E., GOMES, J., GIORDANO, F., RUSHMEIER, H. E., BERNARDINI, F., AND MAGERLEIN, K. 2003. Scanning and processing 3D objects for web display. In *Proc. Int. Conf. 3D Digital Imaging and Modeling (3DIM)*, 310–317.

FIGUEIREDO, M., NOWAK, R., AND WRIGHT, S. 2007. Gradient projection for sparse reconstruction: Application to compressed sensing and other inverse problems. *IEEE J. Selected Topics in Signal Processing 1*, 4, 586–597.

FISCHER, C., AND KAKOULLI, I. 2006. Multispectral and hyperspectral imaging technologies in conservation: current research and potential applications. *Reviews in Conservation 7*, 3–16.

HABEL, R., KUDENOV, M., AND WIMMER, M. 2012. Practical spectral photography. *Comput. Graph. Forum 31*, 2, 1–10.

HART, N. S. 2001. The visual ecology of avian photoreceptors. *Progress in Retinal and Eye Research 20*, 5, 675–703.

HOLROYD, M., LAWRENCE, J., AND ZICKLER, T. 2010. A coaxial optical scanner for synchronous acquisition of 3D geometry and surface reflectance. *ACM Trans. Graph. (Proc. SIGGRAPH 2010) 29*, 3, 99:1–12.

ISO. 2000. Photography – electronic still-picture cameras – resolution measurements. Tech. Rep. ISO 12233:2000, International Organization for Standardization (ISO).

KAWAKAMI, R., WRIGHT, J., TAI, Y.-W., MATSUSHITA, Y., BEN-EZRA, M., AND IKEUCHI, K. 2011. High-resolution hyperspectral imaging via matrix factorization. In *Proc. IEEE Conf. Comput. Vision and Pattern Recognition*, 2329–2336.

KITTLE, D., CHOI, K., WAGADARIKAR, A., AND BRADY, D. J. 2010. Multiframe image estimation for coded aperture snapshot spectral imagers. *Appl. Opt. 49*, 36, 6824–6833.

LABSHPERE, 2011. Spectralon diffuse reflectance standards. http://www.labsphere.com/uploads/datasheets/diffusereflectance-standards-product-sheet.pdf.

LAND, M. F., AND NILSSON, D.-E., Eds. 2002. *Animal Eyes*. Oxford University Press, Oxford.

LENSCH, H., KAUTZ, J., GOESELE, M., HEIDRICH, W., AND SEIDEL, H. 2003. Image-based reconstruction of spatial appearance and geometric detail. *ACM Trans. Graph. (Proc. SIGGRAPH 2003) 22*, 2, 234–257.

LEVOY, M., PULLI, K., CURLESS, B., RUSINKIEWICZ, S., KOLLER, D., PEREIRA, L., GINZTON, M., ANDERSON, S. E., DAVIS, J., GINSBERG, J., SHADE, J., AND FULK, D. 2000. The digital Michelangelo project: 3D scanning of large statues. In *Proc. SIGGRAPH 2000*, 131–144.

MANSOURI, A., LATHUILIERE, A., MARZANI, F. S., VOISIN, Y., AND GOUTON, P. 2007. Toward a 3D multispectral scanner: An application to multimedia. *IEEE Multimedia 14*, 1, 40–47.

MCGRAW, K. J. 2006. Mechanics of uncommon colors in birds: pterins, porphyrins, and psittacofulvins. In *Bird coloration, Vol. I, Mechanisms and measurements*, G. E. Hill and K. J. Mcgraw, Eds. Harvard University Press, Cambridge, Massachusetts.

NEWSOME, D., AND MODRESKI, P. 1981. The colors and spectral distributions of fluorescent minerals. *J. the Fluorescent Mineral Society 10*, 7–56.

NEXT-LIMIT-TECHNOLOGIES, 2012. Maxwell Render. http://www.maxwellrender.com/.

NVIDIA, 2012. About iRay, physically correct GPU rendering technology. http://www.mentalimages.com/products/iray/about-iray.html.

QIN, J. 2010. Hyperspectral imaging instruments. In *Hyperspectral Imaging for Food Quality Analysis and Control*, D.-W. Sun, Ed. Elsevier, 129–175.

RAPANTZIKOS, K., AND BALAS, C. 2005. Hyperspectral imaging: potential in non-destructive analysis of palimpsests. In *Proc. Int. Conf. Image Processing (ICIP)*, vol. 2, 618–621.

SAUNDERS, D., AND CUPITT, J. 1993. Image processing at the National Gallery: The VASARI project. *National Gallery Tech. Bull. 14*, 72–86.

STODDARD, M. C., AND PRUM, R. O. 2008. Evolution of avian plumage color in a tetrahedral color space: a phylogenetic analysis of new world buntings. *The American Naturalist 171*, 6, 755–776.

STODDARD, M. C., AND PRUM, R. O. 2011. How colorful are birds? Evolution of the avian plumage color gamut. *Behavioral Ecology 22*, 5, 1042–1052.

SUGIURA, H., KUNO, T., WATANABE, N., MATOBA, N., HAYASHI, J., AND MIYATA, Y. 2000. Development of a multispectral camera system. In *Proc. SPIE 3965*, 331–339.

SUN, X., AND PITSIANIS, N. 2008. Solving non-negative linear inverse problems with the NeAREst method. *Proc. SPIE 7074*, 707402.

THOURY, M., ELIAS, M., FRIGERIO, J. M., AND BARTHOU, C. 2005. Non-destructive identification of varnishes by UV fluorescence spectroscopy. In *Proc. SPIE 5857*, 1–11.

VOS, J. J. 1978. Colorimetric and photometric properties of a 2-deg fundamental observer. *Color Res. Appl. 3*, 125–128.

WAGADARIKAR, A., JOHN, R., WILLETT, R., AND BRADY, D. J. 2008. Single disperser design for coded aperture snapshot spectral imaging. *Appl. Opt. 47*, 10, B44–B51.

WAGADARIKAR, A. A., PITSIANIS, N. P., SUN, X., AND BRADY, D. J. 2009. Video rate spectral imaging using a coded aperture snapshot spectral imager. *Opt. Express 17*, 8, 6368–6388.

WARE, G., CHABRIES, D., CHRISTIANSEN, R., BRADY, J., AND MARTIN, C. 2000. Multispectral analysis of ancient Maya pigments: implications for the Naj Tunich Corpus. In *Proc. IEEE Geoscience and Remote Sensing Symposium*, vol. 6, 2489–2491.

WRIGHT, S., NOWAK, R., AND FIGUEIREDO, M. 2009. Sparse reconstruction by separable approximation. *IEEE Trans. Signal Processing 57*, 7, 2479–2493.

ZHAO, Y., BERNS, R. S., TAPLIN, L. A., AND CODDINGTON, J. 2008. An investigation of multispectral imaging for the mapping of pigments in paintings. In *Proc. SPIE 6810*, 1–9.